Materials & Design 205 (2021) 109711

Contents lists available at ScienceDirect

Materials & Design

journal homepage: www.elsevier.com/locate/matdes

Enhancing corrosion resistance, hardness, and crack resistance in magnetron sputtered high entropy CoCrFeMnNi coatings by adding carbon

León Zendejas Medina [a,*], Marcus V. Tavares da Costa [b], E. Maria Paschalidou [a], Greta Lindwall [c], Lars Riekehr [a], Marcus Korvela [d], Stefan Fritze [a], Szilárd Kolozsvári [e], E. Kristofer Gamstedt [b], Leif Nyholm [a], Ulf Jansson [a]

[a] Uppsala University, Department of Chemistry – Ångström Laboratory, Uppsala University, Box 538, SE-751 21 Uppsala, Sweden
[b] Uppsala University, Division of Applied Mechanics, Department of Materials Science and Engineering, Box 534, SE-751 21 Uppsala, Sweden
[c] Royal Institute of Technology (KTH), Department of Material Science and Engineering, Brinellvägen 23, SE-100 44 Stockholm, Sweden
[d] Uppsala University, Analytical Chemistry, Department of Chemistry – BMC, Box 599, SE-751 24 Uppsala, Sweden
[e] Plansee Composite Materials GmbH Siebenbürgerstraße 23, DE-86983 Lechbruck am See, Germany

HIGHLIGHTS

- Carbon addition improves corrosion resistance, hardness, and crack resistance.
- Thermodynamic calculations were performed using the Calphad method.
- The calculations predicted carbide formation, and Cr depletion from the alloy phase .
- Carbide formation is suppressed to form a homogenous amorphous phase.

GRAPHICAL ABSTRACT

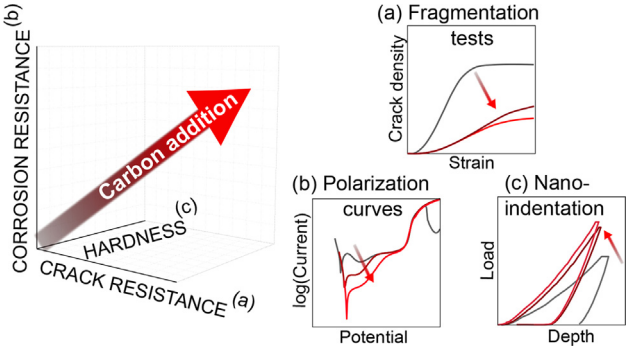

ARTICLE INFO

Article history:
Received 20 November 2020
Revised 30 March 2021
Accepted 1 April 2021
Available online 9 April 2021

Keywords:
Thin film
Magnetron sputtering
Corrosion
Fragmentation test
Amorphous alloys
Bipolar plate

ABSTRACT

This study explores carbon addition as a materials design approach for simultaneously improving the hardness, crack resistance, and corrosion resistance of high entropy thin films. CoCrFeMnNi was selected as a starting point, due to its high concentration of weak carbide formers. The suppression of carbides is crucial to the approach, as carbide formation can decrease both ductility and corrosion resistance. Films with 0, 6, and 11 at.% C were deposited by magnetron co-sputtering, using a graphite target and a sintered compound target. The samples with 0 at.% C crystallized with a mixture of a cubic closed packed (ccp) phase and the intermetallic χ-phase. With 6 and 11 at.% C, the films were amorphous and homogenous down to the nm-scale. The hardness of the films increased from 8 GPa in the carbon-free film to 16 GPa in the film with 11 at.% C. Furthermore, the carbon significantly improved the crack resistance as shown in fragmentation tests, where the crack density was strongly reduced. The changes in mechanical properties were primarily attributed to the shift from crystalline to amorphous. Lastly, the carbon improved the corrosion resistance by a progressive lowering of the corrosion current and the passive current with increasing carbon concentration.

© 2021 The Author(s). Published by Elsevier Ltd. This is an open access article under the CC BY license (http://creativecommons.org/licenses/by/4.0/).

* Corresponding author: Department of Chemistry – Ångström Laboratory, Uppsala University, Box 538, SE-751 21 Uppsala, Sweden.
E-mail address: leon.zendejas.medina@kemi.uu.se (L. Zendejas Medina).

https://doi.org/10.1016/j.matdes.2021.109711
0264-1275/© 2021 The Author(s). Published by Elsevier Ltd.
This is an open access article under the CC BY license (http://creativecommons.org/licenses/by/4.0/).

1. Introduction

CoCrFeMnNi, also known as the Cantor alloy, is a material in the class of high entropy alloys (HEAs) [1]. It was one of the first to be classified as such and is now one of the most well-studied HEA systems [2]. HEAs are defined as alloys of at least four metallic elements at close to equal atomic concentrations, and they characteristically form a single phase with a simple crystal structure. CoCrFeMnNi typically forms a single cubic close-packed (ccp) phase at high temperatures (often referred to as face-centered cubic (fcc)), but multiple phases can form when synthesizing at a lower temperature or during annealing [3,4]. In our previous work, we have observed that sputtering the alloy at room temperature forms metastable phases limited by the low rates of elemental diffusion; in our case ccp and the intermetallic χ-phase (I-43 m) [5]. CoCrFeMnNi is interesting due to its mechanical properties, including a high fracture resistance at cryogenic temperatures [6], and has exhibited a similar passivation mechanism to that of stainless steel, through the formation of a chromium oxide-rich surface film [7]. Compared to steel, it contains higher concentrations of the more expensive elements, such as Co and Ni, so one way to use the material while limiting the costs is to deposit it as a thin film on lower-cost substrates. In this study, we will explore its use as a magnetron sputtered thin film for corrosion protection, and simultaneously modifying several material properties by adding carbon.

A growing field in need of new corrosion-resistant materials is that of polymer electrolyte membrane (PEM) fuel cells, the most common fuel cell in hydrogen vehicles. Due to the low pH inside the cell and the variable voltage during operation, steel components, such as the bipolar plates, undergo corrosion, causing a degradation of the cell performance. The low durability of these materials has become one of the limiting factors for the widespread use of fuel cell technology [8]. To improve the lifetime of the cells, bipolar plates can be coated with thin films to increase their corrosion resistance [9]. The corrosion resistance must, however, be combined with additional material requirements. In many cases, a roll-to-roll deposition of stainless-steel substrates is applied to reduce the manufacturing cost. The flow channels must then be created post-deposition by stamping, meaning that the films need to be highly formable to avoid crack formation. They must also resist scratches and wear. The films must, therefore, meet high demands regarding corrosion resistance, hardness, and crack resistance. This combination of properties is versatile, but rare, as there is typically a trade-off between the hardness and ductility of materials. We have selected equimolar CoCrFeMnNi thin films deposited by magnetron sputtering as a starting point in the search for a multifunctional material that meets the above-mentioned three requirements.

The materials design approach we will explore is the addition of carbon to the films by co-sputtering. Carbon addition to this alloy has as yet only been tested with bulk techniques. Chen et al. [10] studied the addition of up to around 4 at.% C to bulk samples of CoCrFeMnNi, and observed an increase in strength with increasing carbon content, attributed to interstitial and precipitation hardening. The ductility also increased up to 1 at.% C, which was explained by a formation of twins that postponed necking during the tensile tests, something that would not necessarily benefit the tensile strength of coatings. However, at higher carbon concentrations, the carbide precipitation embrittled the material [10]. In sputtered Cr films, carbon has been shown to improve corrosion resistance, by forming a protective carbon-enriched layer that inhibits the corrosion [11]. However, in the case of CoCrFeMnNi, the formation of a crystalline carbide leads to a segregation of the elements, including the depletion of Cr from the alloy phase [10]. Since Cr is the main passivating element, this could lead to preferential corrosion of the Cr-depleted regions. This effect was seen in CoCrFeMnNi bulk samples with 0.5 at.% C, where the Cr-depletion was detrimental to the pitting corrosion resistance [12].

The low solubility of C in CoCrFeMnNi, leading to carbide precipitation, clearly limits the benefits of carbon addition, as both the ductility and the corrosion resistance decrease after adding only a few at.% C due to the Cr-rich carbide. This limitation can be overcome by sputter deposition. During sputtering, the atoms are rapidly quenched from the gas to a solid phase, so that the phase formation often is governed by diffusion kinetics, and metastable phases can be obtained. This has already been used as a strategy to overcome the trade-off between hardness and crack resistance for both single element [13] and HEA [14–16] thin films, where the formation of carbides was suppressed in favor of supersaturated solid solution of carbon in the alloy. Carbon addition to the CoCrFeMnNi system is particularly interesting as it consists of only relatively weak carbide formers, and the known carbides all have complex structures with large unit cells that would require considerable atomic diffusion to form [17]. We expect the high concentration of weak carbide formers to increase the chance of carbide suppression.

While there is a range of widely accepted techniques for quantifying corrosion resistance, suitable methods are still under discussion regarding the mechanical characterization of thin films. To quantify the elastic properties and hardness, nanoindentation is typically used, most often applying the Oliver and Pharr method to calculate hardness and Young's modulus [18–20]. This method assumes an elastic–plastic behavior of the film and is therefore not applicable in the case of fracture. Quantitative measures such as the ratios H/E or H^3/E^2 have been used as proxies for the fracture toughness, but the correlation between these ratios and the number of cracks has only been proven for a few brittle material systems [21]. Cracking caused by nanoindentation can be analyzed [22] but is complicated due to the complex stress states and the influence from the substrate [23]. More direct approaches are available, but require extensive sample preparation and are not useful for films thinner than a few microns [24].

There is clearly a need for a simple way of characterizing fracture behavior of thin and ductile films. In this study, we will explore fragmentation testing of the films on polymer substrates. The coated substrates are stretched inside an electron microscope, and observations are made on the cracking behavior during increasing uniaxial stress. Such a cracking mechanism has been observed for a variety of film materials and thicknesses [25–27]. Considerable fracture data can be generated from only one fragmentation test, and the tensile strength distribution [28] and fracture toughness [29] of the films can be estimated. The simplicity of the test and the range of possible material systems makes it a suitable choice in this study case.

In this work, we evaluate carbon addition to CoCrFeMnNi thin films, as a way to increase the hardness, crack resistance, and corrosion resistance of the material. The phases of the CoCrFeMnNi(C) system are evaluated through thermodynamic calculations with the Calphad method. Thin films of equimolar CoCrFeMnNi with up to 11 at.% C are deposited using magnetron co-sputtering and characterized using diffraction, electron microscopy, and photoelectron spectroscopy. To study the elastic properties and hardness, nanoindentation is used, and we test and evaluate fragmentation tests on a coated polymer substrate as a method for studying the crack resistance. Electrochemical tests and analyses of the electrolytes with inductively coupled plasma mass spectrometry are used to evaluate the corrosion resistance.

2. Experimental

2.1. Thermodynamic calculations

The Calphad approach is a method to describe phase-based properties in multicomponent, multiphase materials systems which has been extensively applied to describe the thermodynamic properties of alloys. In the case of Calphad thermodynamics, it is the Gibbs free energy of each phase that is computed, and the resulting Gibbs free energy expressions are then stored in databases. Calculations where thermodynamic information is needed as input; e.g., calculations of multicomponent equilibrium phase diagrams, can then be performed. In the current work, Calphad thermodynamic calculations were used to obtain the phase fractions and phase compositions for the CoCrFeMnNi(C) system at equilibrium. For this, the Thermo-Calc software packages [30] and the Calphad thermodynamic database for HEAs, version three, from Thermo-Calc [31,32] (TCHEA3) were applied. The obtained results were used as guidance when interpreting the experimental data.

2.2. Synthesis

Thin films were deposited through unbalanced dc magnetron sputtering, using a graphite target from Kurt J Lesker (99.999% pure) and a composite CoCrFeMnNi target from Plansee Composite Materials, Germany. The CoCrFeMnNi targets were produced by spark plasma sintering, mixing powders of the five elements with average grain sizes between 10 and 45 μm and maximum grain size of 80 μm. Sintering was performed in vacuum for 10 min at 780 °C, applying a pressure of 30 MPa to the powders in a graphite mold. The short sintering time allowed a dense and fine-grained material to form, without alloying or formation of intermetallic phases, which might aggravate the machining of the targets. The resulting targets were equimolar, as quantified by X-ray fluorescence spectroscopy (XRF), 98.5% pure (at.%) with contamination of mainly oxygen, and had a density of 7,5 g/cm^3. As for the film deposition, the method is described in a previous publication [5], detailing the deposition geometry, pressure and flow of Ar gas, substrate rotation, and handling of the substrates. In this study, no active heating was used, which resulted in a varying substrate temperature of 20 to 85 °C, the metal target power was 150 W and a substrate rf bias of −100 V was selected. The target power of the graphite target was then varied to obtain different carbon contents, while all other sputter parameters were held constant. These synthesis parameters, particularly a high substrate bias for all samples, were selected to obtain a sample series with a dense microstructure and to minimize variations in surface roughness. This is required to obtain a high corrosion resistance and comparable results throughout the sample series. The deposition time was around 60 min, resulting in films of approximately 500 nm thickness. All films were deposited on two types of substrates, Si substrates with a 1.5 μm thick amorphous oxide grown by dry oxidation, chosen to facilitate the characterization of the crystal structure by diffraction, and 4 by 11 mm polyimide strips suitable for the fragmentation tests.

2.3. Characterization

2.3.1. Composition, structure, and morphology

The morphology of the films was studied with scanning electron microscopy (SEM). Cross-section electron images were recorded in a Zeiss Merlin instrument using the in-lens detector and a field emission gun (FEG) operating at 3–5 kV acceleration voltage. The relative concentrations of all five metallic elements were recorded by energy-dispersive X-ray spectroscopy (EDX), using an 80 mm^2 silicon drift detector in a Zeiss 1530 instrument with a voltage of 15 kV, and analyzed using the Aztec (INCA energy) software.

The carbon and oxygen concentrations were measured using X-ray photoelectron spectroscopy (XPS) sputter profiles, in a PHI *Quantera* II 2000 scanning XPS microprobe with monochromatic Al K_α radiation. The analysis area was 100 μm^2, and the samples were etched using 200 eV Ar^+ ions in steps, after which the bulk concentration was calculated by averaging three steps with stable peak intensities. The C 1 s and O 1 s peaks were used to calculate the relative concentrations, using sensitivity factors determined with time-of-flight elastic recoil detection analysis (ToF-ERDA) using two standard samples of similar composition. The same instrument was used to record high-resolution spectra of the bulk film after the sputter ion etching.

The crystalline phase content of the films was studied using grazing incidence X-ray diffraction (GI-XRD) in 0.02° steps with 2 s/step, on a Siemens D5000 instrument with parallel Göbel mirror and parallel plate collimator with 0.4° divergence.

Cross-sections of the samples with 0 at.% and 11 at.% carbon were prepared for transmission electron microscopy (TEM) analysis using a focused ion beam in a scanning electron microscope (FIB-SEM, FEI Strata DB235). The samples were then mounted on a Cu lift-out grid and a focused 30 kV Ga ion beam was used to thin them to electron transparency. This was followed by a polishing step using 5 kV Ga ions to reduce the thickness of the surface damaged volume. The TEM analysis was performed at 200 kV with a probe corrected FEI Titan Themis equipped with the SuperX system for EDX. Selected area electron diffraction (SAED) patterns and hollow cone dark field (HCDF) images were recorded in the TEM mode. The SAED patterns were evaluated with the programs CrystBox [33] and JEMS [34]. EDX maps were acquired in the scanning TEM (STEM) mode and evaluated with the software ESPRIT 1.9 by Bruker.

2.3.2. Mechanical tests

Nanoindentations were performed with a CSM instrument. A Berkovich diamond tip was used to evaluate the hardness and elastic modulus of the films with indents performed at a loading rate of 2.5 mN/min down to a depth of 50 nm, which corresponded to approximately 10% of the film thickness. The indentation hardness, H, and reduced Young's modulus, E_r, were calculated using the Oliver-Pharr method [20]. A cube corner diamond tip was then used to study the deformation qualitatively by performing indents of different depths down to 1250 nm, e.g. more than twice the film thickness, at a rate of 5 mN/min. The cube-corner tip was used to achieve a higher strain for the same load compared to the Berkovich tip, thus increasing the probability of crack formation. These indents were studied with SEM imaging in the Zeiss Merlin instrument described in 2.3.1., using a secondary electron detector and different sample tilts. For both types of indents, load control and an acquisition rate of 10 Hz were used, and the tips were calibrated with Al_2O_3.

To qualitatively study the crack resistance of the samples in the carbon series, in situ fragmentation tests [28] were carried out. The tests were performed using a Hitachi scanning electron microscope operating at 15 kV acceleration voltage and a Deben tensile stage, on samples deposited on 4x10 mm^2 polyimide strips. The samples were stretched using a displacement rate of 0.1 mm/min while monitoring in-situ the crack accumulation in the coating. Fragmentation diagrams were obtained by plotting the crack density, CD, as a function of tensile strainε. The fragmentation diagram is represented by the empirical cumulative distribution function or probability of failure in the fragmentation tests (except close to crack saturation) [25]

$$F_\infty = CD(\sigma)/CD_\infty \approx 1 - \exp\left[-(\sigma/\sigma_\infty)^\rho\right] \quad (1)$$

where σ is the thin film stress and ρ and σ_∞ are the Weibull shape and scale parameters, respectively. Here, the thin film strength and the experimental scatter are represented by Weibull parameters [35]. Another way to measure the crack resistance is by using fracture mechanics. The main material property is the fracture energy or the critical energy release rate [29]

$$G = \pi/2\ h\bar{E}\,\varepsilon_{onset}^2 g(\alpha_D, \beta_D) \quad (2)$$

at the crack onset strain (COS), where h is the thickness of the thin film, $\bar{E} = E_c/(1 - \nu_c^2)$ is the plane strain tensile modulus of the thin film, $\varepsilon_{\text{onset}}$ the crack onset strain whereas $g(\alpha_D, \beta_D)$ is a dimensionless function of the Dundurs parameters [36]. In this section, the residual stresses of the thin films were not considered since the deposition was carried out at room temperature. The fragmentation tests were also performed several days after the coating deposition, allowing stress relaxation in the polymer substrate.

2.3.3. Electrochemical tests

In the electrochemical experiments, a three-electrode electrochemical cell was used in connection with an SP-300 BioLogic potentiostat (BioLogic Science Instruments). A 0.05 M H_2SO_4 aqueous solution served as the electrolyte and the thin film samples were used as working electrodes. The reference electrode was an Ag/AgCl (3 M NaCl) reference electrode (RE) whereas a Pt wire functioned as the counter electrode (CE). All measurements were performed at room temperature. Firstly, the samples were kept in the electrolyte solution for 40 min under open circuit potential (OCP) conditions, after which the electrolyte was collected and analyzed with inductively coupled plasma mass spectrometry (ICP-MS). Electrochemical impedance spectroscopy (EIS) measurements were then carried out at the OCP within an applied frequency range from 100 kHz (initial frequency) to 100 mHz (final frequency), using an ac amplitude of 10 mV. The recorded spectra were plotted as Nyquist plots. Following that, potentiodynamic polarization curves were recorded to evaluate the corrosion resistance of the films. A potential range from −0.3 vs. the OCP to 1.5 V vs. Ag/AgCl and a scan rate of 5 mV/s were used in these tests. Additionally, chronoamperometry (CA) experiments were performed on the samples, for two hours at 0.4 V and 1.3 V vs. Ag/AgCl respectively, after which the electrolyte was subjected to ICP-MS analyses. The ICP-MS analysis method is described in the supporting methods.

3. Results and discussion

3.1. Thermodynamic calculations

The elemental compositions of the samples are presented in Table 1; three compositions containing 0, 6, and 11 at.% C, respectively, were chosen for analysis. Using the Calphad method, the phase fractions and phase compositions at equilibrium were calculated for the three sample compositions. For the carbon-free samples, the calculations agreed with several examples in the literature [3], predicting a single ccp phase above 800 °C and phase mixture of a ccp phase, a σ-phase, and a bcc phase below this temperature.

Fig. 1(a) and (b) show the equilibrium phases for 6 and 11 at.% C, respectively, as a function of the temperature. For both compositions, the predicted phases at temperatures above 600 °C are a ccp phase and the metal carbide M_7C_3. This carbide has a complex hexagonal structure (space group $P6_3mc$), with a unit cell containing 80 atoms. In Fig. 1 (c) and (d), the compositions of the M_7C_3 carbide as a function of the temperature are shown. The carbide consists of 30 at.% C, 50–70 at.% Cr (lower Cr concentration is seen for higher carbon content) and small amounts of the remaining elements, with Mn and Fe being slightly more abundant than Co and Ni. This agrees with the results obtained by Chen et al. for 2–4 at.% C [10]. It is also in line with current knowledge on carbide formation as Cr and Mn are known to form thermodynamically stable carbides, while the carbides of Fe, Co, and Ni are metastable [37]. Furthermore, the carbon affinity decreases with increasing group number for the d-block elements [17]. The ccp phase (presented in Fig. 1 (e) and (f)) is depleted of Cr and contains only a few at.% C. An FeCo-rich bcc phase appears below 600 °C for both compositions and consists of around 45 at.% of each metallic element, with about 10 at.% C. Lastly, with 6 at.% C, a σ-phase with the approximate formula $Cr_{21}Mn_{32}Fe_{31}Co_{14}Ni_2$ is found below 500 °C. With 11 at.% C, the σ-phase is not present, and instead, a second metal carbide with the formula Cr_3C_2 is formed below 600 °C (orthorhombic, space group Pnma).

The Thermo-Calc Software TCS High Entropy Alloys Database version 3 (TCHEA3), which was used for the present calculations, includes thermodynamic assessments of the full temperature and compositional range of all the binary sub-systems of the included elements. It also includes assessments of eleven out of twenty of the ternary sub-systems, including six of the ternary metal–carbon systems. While a lot of work has been published on thermodynamic calculations of the phases in HEAs [38] and some work specifically validating the calculation on the CoCrFeMnNi system [3], there are only a few examples of calculations of multicomponent systems with added carbon [39–41]. To support the calculations in this paper, we have compiled the observed phases in known bulk studies of CoCrFeMnNi with added carbon and compared them to the equilibrium phases calculated using the TCHEA3 database. The list can be found in the Supporting Results (SI Table 2). A section of the phase diagram with varying C content and equiatomic CoCrFeNiMn, with up to 10 at.% C is also presented (SI Fig. 1). The experiments and calculations show relatively good agreement. A single ccp phase with interstitial carbon is stable at up to 0.8 at.% C at 1200 °C and the solubility decreases with decreasing temperature. At higher carbon concentrations, a phase mixture of ccp and the carbide M_7C_3 is expected, and at lower temperatures, a σ phase and a $M_{23}C_6$ carbide are stable. From this first assessment of validity, we can conclude that the calculations and experiments show relatively good agreement in samples with a few at.% C, and that they correctly predict phase equilibria with metal carbides at carbon concentrations higher than 0.8 at.%. It should be noted that, due to the lack of thermodynamic data at low temperatures, a prediction of the equilibrium phases at the synthesis temperature (20–85 °C) with the Calphad method would

Table 1
The atomic composition of all films measured by EDS and XPS.

C target	Concentration (at.%)					
Power (W)	**Cr**	**Mn**	**Fe**	**Co**	**Ni**	**C**
0	18	18	21	21	22	0
87	18	13	21	21	21	6
167	18	10	20	20	21	11

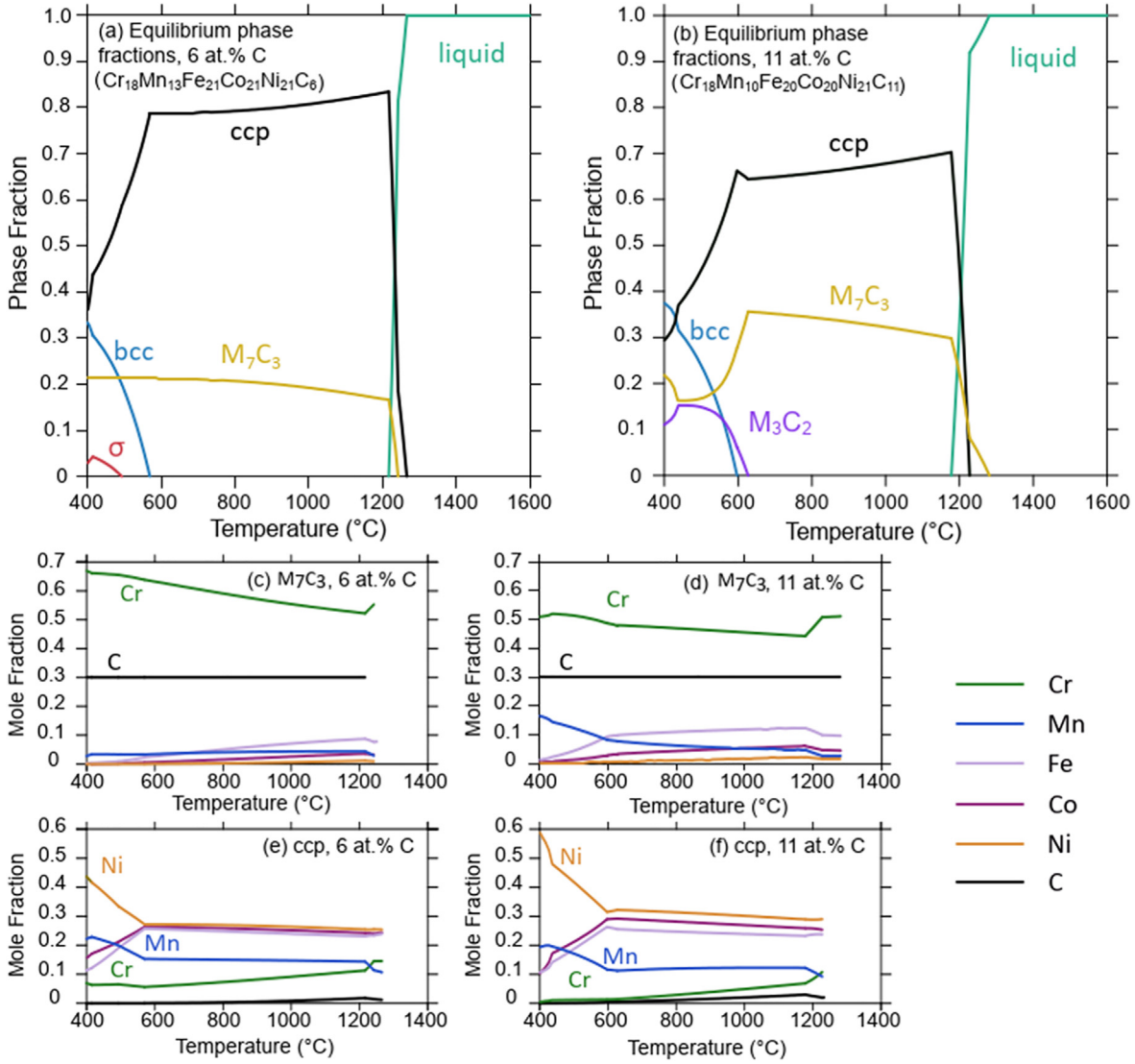

Fig. 1. The results from Calphad thermodynamic calculations for the equimolar CoCrFeMnNi system with 6 and 11 at.% added carbon, following the compositions in Table 1. (a-b) the predicted phase fractions, (c-d) the composition of the M_7C_3 phase, and (e-f) the composition of the ccp phase, as a function of the temperature.

Table 2
Summary of material properties for the sample series, sorted with respect to the characterization technique.

	Nanoindentation[a]			Fragmentation tests[b]			Polarization curves		
Sample ID	**HIT (GPa)**	**E_r (GPa)**	**COS (%)**	**σ_∞ (GPa)**	**ρ (-)**	**G (J/m²)**	**E_{corr} (V)**	**j_{corr} (A/cm²)**	**$j_{passive}$[c] (A/cm²)**
0 at.% C	7.9 ± 0.4	180 ± 5	0.62 ± 0.06	2.0	2.8	31 ± 8	−0.28	$8{\cdot}10^{-6}$	$1{\cdot}10^{-5}$
6 at.% C	14.1 ± 0.6	173 ± 4	0.8 ± 0.3	3.8	2.5	44 ± 42	−0.21	$9{\cdot}10^{-7}$	$2{\cdot}10^{-6}$
11 at.% C	15.9 ± 0.6	183 ± 2	1.1 ± 0.2	3.9	2.4	86 ± 51	−0.18	$8{\cdot}10^{-8}$	$5{\cdot}10^{-7}$

Abbreviations: HIT: indentation hardness, E_r: reduced Young's modulus, COS: crack onset strain, σ_∞: Weibull scale parameter, ρ: Weibull shape parameter, G: fracture energy, E_{corr}: corrosion potential, j_{corr}: corrosion current density, $j_{passive}$: passive current density.
[a] The uncertainties are the standard deviations from 20 indentations performed on one sample.
[b] The uncertainties are the standard deviations from tensile tests on three separate samples.
[c] (at 0 V vs. Ag/AgCl).

be uncertain. The results from this section can only be used to predict the results of annealing or synthesis at higher temperatures.

Based on these results, it would not be possible to achieve carbon-containing CoCrFeMnNi with the desired qualities through traditional bulk methods, such as melting or casting. The formation of the M_7C_3 and M_3C_2 carbides, although it might increase the hardness, would embrittle the material. The segregation of the metallic elements, particularly the depletion of Cr from the alloy phases, would likely lead to more rapid corrosion of these phases, as they cannot form the passivating Cr-rich surface oxide [42].

3.2. Composition, structure, and morphology

As can be seen in Table 1, the films sputtered with an equimolar composite target displayed close to equimolar ratios for the carbon-free samples, with a slightly lower concentration for the lighter elements and vice versa. The concentration of Mn decreases greatly

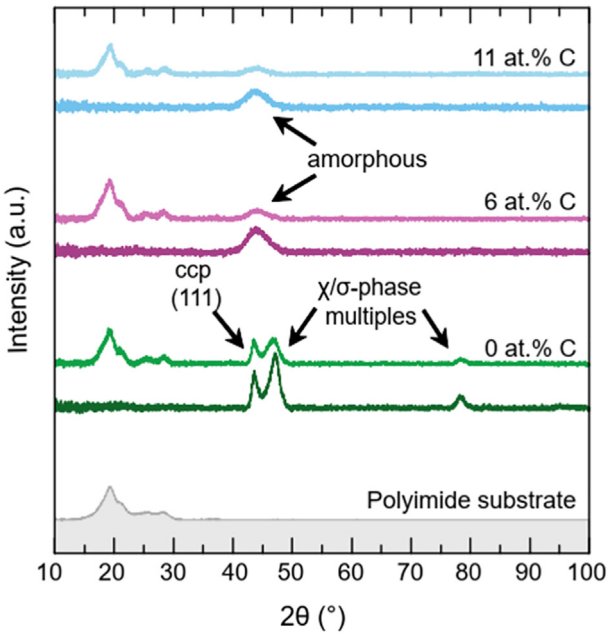

Fig. 2. Results from GI-XRD measurements of the samples. The darker line for each composition denotes films deposited on oxidized Si whereas the lighter lines represent films deposited on polyimide. The diffractogram for the polyimide substrate is shown in grey color at the bottom of the graph. All intensities are background subtracted.

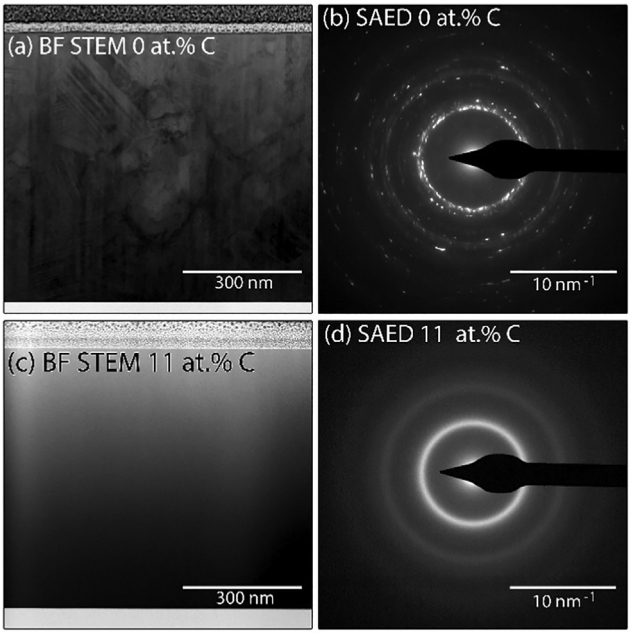

Fig. 3. Bright-field STEM images and the corresponding SAED patterns of a)-b) the sample with 0 at.% C, and c)-d) the sample with 11 at.% C.

with increasing carbon content. This was linked to the increase in the graphite target power during the deposition combined with the use of the rf substrate plasma, probably leading to a change in the plasma density close to the growing film. This in turn appears to have led to faster preferential sputtering of Mn. It is not clear why the plasma conditions affected Mn to a greater extent, but it may be of importance that it is the most volatile of the five metallic elements, that it has the most rapid diffusion within this alloy [43], and, as we and other groups have reported [5,44], that it tends to segregate to the grain boundaries in the material. The oxygen content in all the films was below 1 at.% in the bulk.

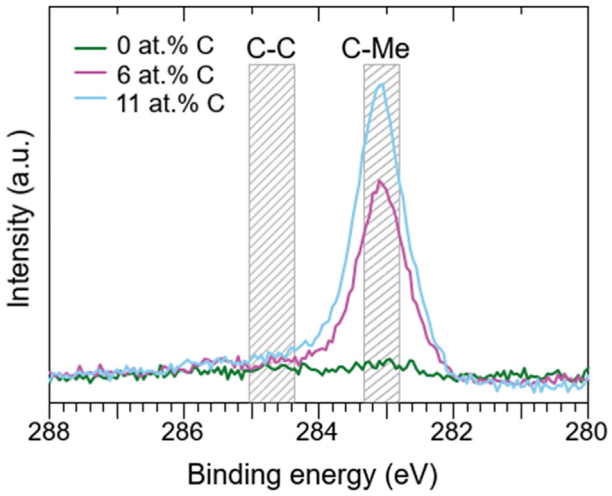

Fig. 4. Core-level XPS spectrum of C1s peak. The striped regions indicate the energy intervals given in the literature for the C-C [49] and the C-Me [46–48] binding energies.

In Fig. 2 the effect of the carbon on the crystal structure is presented. The structures appeared to be the same on the oxidized Si and the polyimide substrates. For the carbon-free samples, a phase mixture of ccp and χ-phase was found, as shown by the ccp(1 1 1) peak and clusters of multiple χ-phase peaks. The identification of the crystalline phases, which was done by a combination of selected area electron diffraction (SAED) and XRD, is explained in a previous publication [5]. Although ccp and χ-phase were the main identified phases, a σ-phase could not be excluded. The two carbon-containing samples appeared X-ray amorphous and no evidence of a crystalline carbide phase was found.

The SAED patterns depicted in Fig. 3(b) and (d) confirm the change from crystalline to amorphous, as is also apparent from the lack of contrast in the bright field STEM images (Fig. 3(c)). The same change in morphology is depicted in the tilted cross-section SEM micrographs of the films, presented in the supplemental results (SI Fig. 2). After the addition of carbon, the films are smooth and appear free from grain boundaries or other features at this degree of magnification (250 k x), an effect tied to the amorphous nature of the films. The fracture surface of the 11 at.% C sample exhibits the typical vein pattern caused by shear band formation [45]. The EDX results for the films with 0 at.% and 11 at.% C, shown in the supporting information (SI Fig. 3), display a uniform distribution of the elements down to the nm-scale.

The core-level XPS C1s spectra in Fig. 4 show peaks at 283.1 eV for the samples with added carbon, a binding energy typical for a carbidic environment in amorphous Me-C films of similar composition [46–48]. Little to no contribution from free carbon is found, as seen by some diffuse intensity around 285 eV [49]. It can therefore be concluded that the carbon is fully incorporated into the amorphous alloy, binding almost exclusively to the metallic elements. Since there is no clear distinction in the nature and bond strength of carbon in metal carbides and in solid solutions, no conclusions could be drawn with XPS alone regarding the formation of a crystalline metal carbide. These results are a complement to the diffraction with XRD and SAED in TEM, which indicate that no such carbide was formed. Neither do these results reveal preferential bonding to any one metallic element. The reported shift in C1s varies more between values reported for the same carbide in different studies (e.g. 282.9–283.5 eV for Cr_7C_3 [50–52]) than between carbides of

the different metals (e.g. 283.3 eV for amorphous Fe-C [48]). A separate study will be published in the near future on the local environment of the carbon, using Hard X-ray Photoelectron Spectroscopy (HAXPES) and Near Edge X-ray Absorption Spectroscopy (NEXAFS). Due to several large overlaps with Auger lines, the 2p spectra of the five metallic elements were not included in the study.

The addition of carbon to sputter-deposited metallic films has been explored for many metals and alloys [15,53]. At low carbon contents, an interstitial solid solution of carbon in the metallic lattice is typically formed. The extent of carbon solubility varies with the metallic element as well as the crystal structure. As explained in the introduction, the fast quenching during the sputtering can yield a solid solution of carbon with higher carbon content than is thermodynamically favorable, if the formation of this phase requires less atomic diffusion than that of the carbide [13,14]. Beyond a certain carbon concentration, the energy cost of supersaturation is too high and no more carbon will be accommodated into the metal lattice. For metallic elements with high carbon affinities, the formation of a crystalline carbide phase will be more favorable. At even higher carbon contents, the films can become amorphous or they can form a nanocomposite of carbide particles in a carbon matrix [53]. If the alloy contains weaker carbide formers, the formation of a crystalline carbide can be entirely avoided and the carbon concentration required for amorphization is decreased [54]. It should be noted that, while the composition has a great influence on the likelihood of forming amorphous materials, the effect of sputter process parameters cannot be ignored, as they govern the extent of ad-atom diffusion.

The films in our study are amorphous with both 6 and 11 at.% C, with no evidence of the Cr-rich carbide that was predicted by the thermodynamic calculations. This phase was clearly suppressed, following the principles explained above. The effect of the limited atomic diffusion during sputtering could be particularly pronounced for the present composition; the formation of the larger M_7C_3 or M_3C_2 unit cells would require more extensive atomic diffusion, compared to the simple NaCl structures formed by the earlier transition metals.

A fundamental question tied to the phase formation in this study is whether the multicomponent and equimolar composition of the alloy affects the tendency to form amorphous films upon carbon addition. Two examples from the literature suggest that an amorphous material is preferred to a supersaturated solid solution of carbon in equimolar compositions. Firstly, in a parallel to the films in this study, thin films of 316L stainless steel (the composition was $Fe_{69}Cr_{18}N_{i11}Mo_2$) [46] were deposited with carbon added by reactive magnetron sputtering. For these films, a solid solution was reported to be stable with up to 15 at.% C, after which an amorphous material was formed. Analogous results were obtained in a study focusing on magnetron sputtered CrNbTaTiW with added carbon [14,55]. Here, the addition of 8 at.% carbon resulted in an amorphous film for the near-equimolar (slightly Cr-enriched) metal composition, while the same amount of carbon in a non-equimolar TaW-rich composition was dissolved in the metallic lattice. This is an interesting observation, and further studies should be conducted to test if the equimolar alloys exhibit an earlier destabilization of the solid solution compared to conventional alloys.

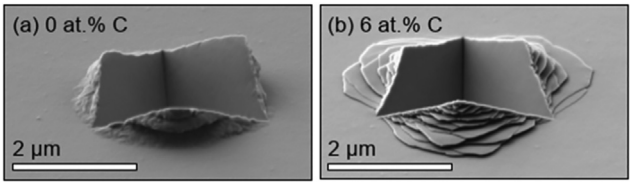

Fig. 5. Secondary electron SEM micrographs of indents performed with a cube corner diamond tip, for 0 at.% and 6 at.% C. The indent depth is 1250 nm, which corresponds to more than twice the film thickness. The samples were tilted 59° with respect to the electron beam.

3.3. Mechanical properties of the films

The nanoindentation results, presented in Table 2, show that the indentation hardness, HIT, increased with the carbon content. The largest increase was seen between the samples with 0 and 6 at.% C, which had hardness values of 7.9 and 14.1 GPa, respectively. A smaller difference was seen between the two carbon-containing samples, though the sample with 11 at.% C was found to be significantly harder (using a two-tailed t-test with $\alpha = 0.01$), with a value of 15.9 GPa. No trend could be discerned regarding the reduced Young's modulus, E_r, which was similar for all three samples. Finally, the ratio H/E increased, from 0.04 to 0.09. As discussed earlier, it is not fully established what the relationship between H/E and the crack resistance is for ductile materials [21]. Nevertheless, the increase suggests an improved fracture toughness.

Fig. 5 shows SEM images of indents obtained using a cube corner tip for the samples with 0 at.% and 6 at.% C. The two carbon-containing samples displayed the same deformation behavior. The indent to 1250 nm, which corresponds more than twice the film thickness, formed no cracks for either sample. Both samples displayed a continuous plastic deformation with pile-up formation (for the indentations at several depths see Supplemental results SI Fig. 4). For the film with 6 at.% C, the pile-up was composed of many bands, indicating a more uneven deformation mechanism. The bands can be related to pop-in events present in the load vs. depth curve (not shown). This serrated flow is typical of metallic glasses [56,57], and each visible band can be related to the activation of a shear band [45]. The absence of cracks shows that this method is not suitable for testing the crack resistance of materials with this high ductility.

To further investigate the mechanical performance of the thin films, fragmentation tests were performed. In Fig. 6, SEM micrographs show representative images of the thin films at different strains during the fragmentation test on polyimide substrates, with cracks appearing perpendicular to the direction of the strain. For the carbon-free sample, the cracks propagated through the entire width of the thin film directly upon crack onset, as shown in microscope images (Fig. 6, upper left), whereas for carbon-containing thin films, the crack propagation was mainly initiated at the edges and propagated progressively across the width of the thin film (Fig. 6, second and third rows). The number of cracks decreased with increasing carbon concentration at all strains, with the most notable difference between the carbon-free thin film and the two amorphous carbon-containing ones.

Fig. 7(a) shows the crack density as a function of tensile strain for the three samples. The dots are experimental data and the solid curve corresponds to the empirical distribution function Eq. (2). A higher density of cracks was found for the carbon-free thin film. The accumulation of many cracks also gives information on the scatter in the strength of the thin film material which is of engineering importance for the mechanical integrity of thin films. The scatter is commonly represented in Weibull plots, from which the distribution parameters can be directly deduced from the slope and intercept of the linear regression line. The offset to higher values for the carbon-free thin film in the Weibull plot in Fig. 7(b) shows a difference in the modal or typical value defined by the scale parameter, σ_∞. The difference in slopes shows a difference in the scatter of the strength, given by the shape parameter ρ. The distribution parameter values are presented in Table 2, with the main result being that both the strength and the scatter are lower for the carbon-free thin film compared with the carbon-containing ones. This indicates that the addition of carbon results in stronger films with a more heterogeneous cracking behavior.

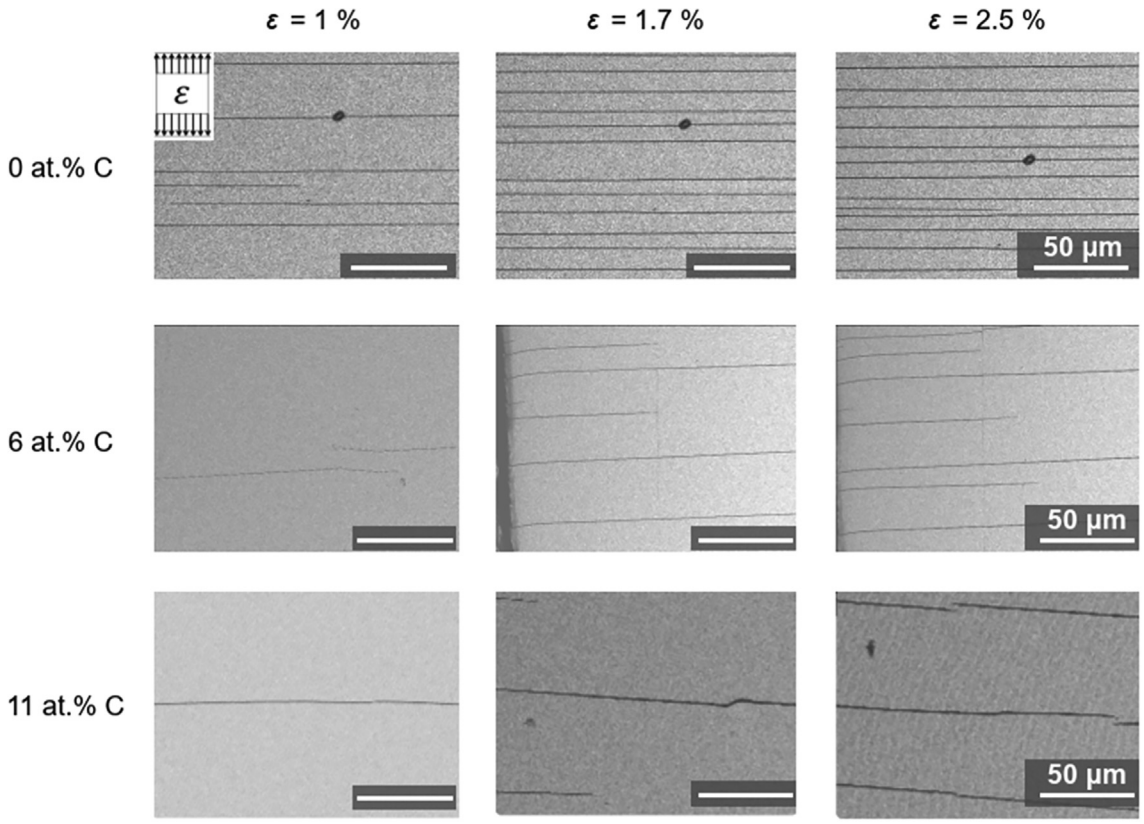

Fig. 6. SEM micrographs of the samples deposited on polyimide substrates. The images are taken during the fragmentation tests to show the cracking evolution at 1%, 1.7% and 2.5% of tensile strain for each carbon content thin film.

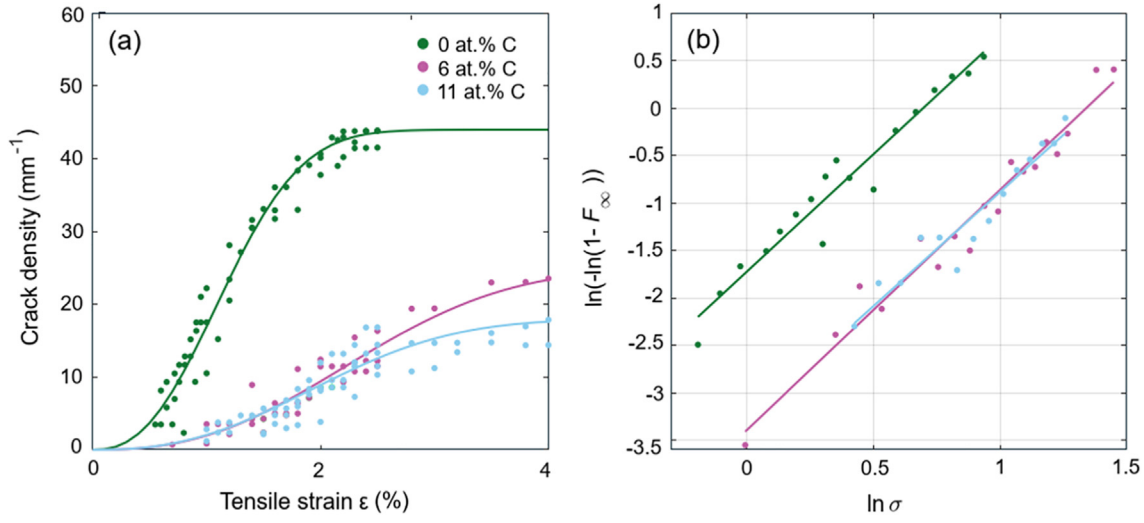

Fig. 7. (a) Fragmentation diagrams for 0% carbon, 6% carbon, and 11% carbon thin films with their correspondent (b) Weibull plots.

The calculated fracture energies at the crack onset, *G*, are reported in Table 2. They suggest an increase in *G* with increasing carbon concentration. However, this change is not statistically significant given the high standard deviation. Large scatter for fracture energy in thin films is not unusual at the crack onset [58,59], since it is typically controlled by the largest flaw. This means that a very large number of samples is needed for comparisons of materials. An F-test ($\alpha = 0.05$), however, showed that there was a significant difference in variance for the crack onset strain between the sample with no carbon compared to the carbon-containing samples. This suggests that the crack formation mechanism is different for these materials.

The observed trends in the mechanical properties of the films can be related to the change in the structure from crystalline to amorphous, causing the plastic deformation mode to change from dislocations to shear banding [45]. Metallic glasses are generally harder than crystalline alloys, and the indents in Fig. 5 display a typical deformation mechanism with activation of individual shear

bands. While metallic glasses are generally known for their low ductility in tensile tests, some exhibit a very high ductility [60]. Another effect that seems to be related to the amorphous nature of the films is the increased scatter in the crack onset strain as well as the continuous formation of cracks, indicating a less predictable cracking behavior. The deformation mechanisms of this system require more in-depth studies, to understand the relatively high crack resistance of the amorphous films and to clarify why the hardness continues to increase with the addition of carbon once amorphous films are already achieved.

3.4. Influence of carbon content on the corrosion resistance

The first step of the corrosion study was a 40-minute-long period at the open circuit potential (OCP), which was about −0.1 V, −0.02 V, and 0.06 V vs. Ag/AgCl for the samples with 0, 6, and 11 at.% C respectively. After this step, the electrolyte was collected, and the metal ion concentrations were determined with inductively coupled plasma mass spectrometry (ICP-MS). The higher OCP values for the carbon-containing samples indicate that the corrosion reactions were slower. The metal ion concentrations are presented in the supporting information (SI Table 3). The overall metal concentration in the electrolyte was found to be 15% lower for the sample with 11 at.% C than for the carbon-free sample. For the samples with both 0 and 11 at.% C, the relative concentrations of Mn and Fe were higher in the electrolytes than in the films (see Table 1), while the relative concentrations of Cr, Co, and Ni were lower in the electrolyte than in the films. The behavior of each element can be related to their electrochemical stabilities [61], and follow a similar trend as seen for stainless steels [62]. In the presence of an acidic aqueous electrolyte, Cr is readily oxidized and forms an oxide (Cr_2O_3) with low solubility, thus passivating the material. Mn and Fe are also easily oxidized but, compared to Cr, form more soluble oxidation products, which appears to have led to their preferential dissolution. Co and Ni have the highest standard potentials and will, therefore, have the lowest driving force for oxidation. As the redox reaction during the OCP is a current-controlled oxidation of the alloy, the metallic elements with the highest driving force will be oxidized preferentially. We can, therefore, expect to find less Co and Ni in their oxidized states.

The conclusions drawn from the ICP-MS results are supported by XPS measurements that were performed on the corroded surface after 40 min at OCP and in the bulk of the films after sputter etching through the corroded layers (see the supporting information, SI Fig. 6). Peak fitting was performed on the 3p region, as the 2p regions have several overlaps with Auger peaks and are therefore unsuitable for this purpose [63]. The results are almost identical for the films with 0 and 6 at.% C. After the 40 min at OCP, Cr is found at higher relative intensities compared to the bulk; it is enriched close to the surface, mainly in its oxidized form. Mn, Fe and Co are partly oxidized while Ni is purely metallic. The contribution from the metallic states of all elements is an indication that the signal is coming partly from below the oxide film and the strong metallic Ni signal suggests that this element is enriched there. Similar results were obtained in a previous XPS depth profiling investigation of the OCP oxide formed in the same electrolyte, where a Cr-rich oxide and an enrichment of Ni below the alloy were found [63]. The carbon was not studied in-depth using XPS, due to the difficulty in separating the carbon signal close to the surface from that of the adventitious carbon, which always is present on the surfaces of metals after their exposure to air [64].

After 40 min at the OCP, electrochemical impedance spectroscopy (EIS) experiments were performed. The results are shown in the Nyquist plots (Fig. 8(a)), and a combined Bode phase and Bode impedance modulus |Z| diagram in the supplemental results (SI Fig. 7). The low-frequency contribution shows the kinetic response for the charge transfer reaction related to a resistance R_{ct}. The phase angle does not reach 90° as it would for ideal capacitive behavior. A comparison of the EIS data in the low-frequency region (100 mHz) shows that the electrochemical interface for the carbon-free sample was dominated by R_{ct}, indicated by a close semi-circle in the Nyquist plot (Fig. 8(a)) and a higher slope of phase angle in the Bode plot at lower frequencies (SI Fig. 7). The carbon-free film under OCP, showed a phase angle close to 71° degrees at the lowest frequency value (100 mHz), while the samples with 6 and the 11 at.% carbon samples exhibit angles of 80.5° and 82.5° degrees respectively. A higher phase shift (closer to 90°) at a lower frequency value in a Bode phase plot is indicative of better corrosion resistance. Similarly, the total impedance magnitude was higher for the samples with carbon and lower for the carbon-free samples at the lowest frequency value. The impedance values increased and became more capacitive when the carbon content was increased in the samples. The electrochemical impedance spectroscopy (EIS) measurements are consistent with the decrease seen in the i_{corr} values since the former were per-

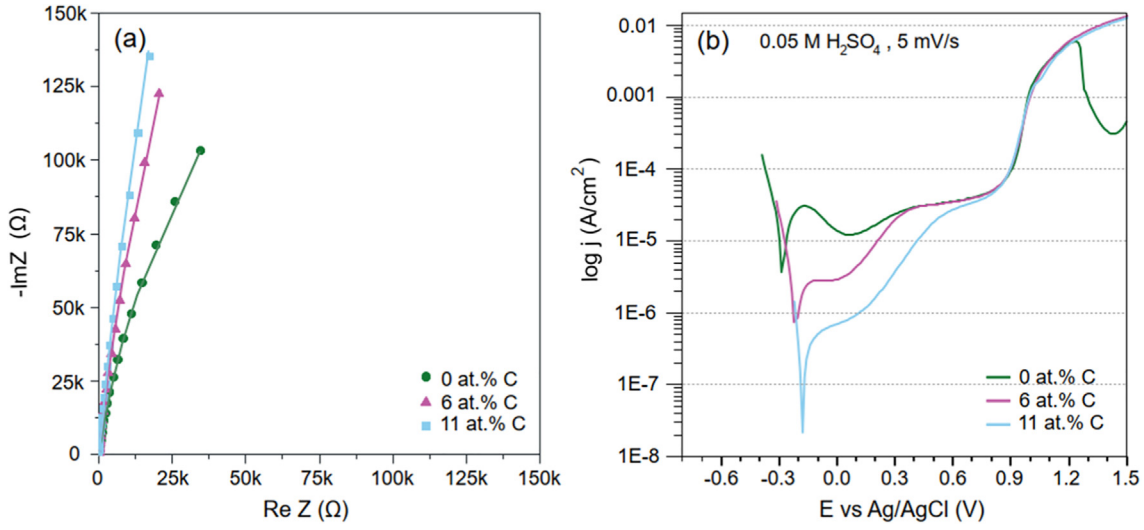

Fig. 8. Electrochemical investigations of the thin film samples with different carbon contents. (a) Nyquist plots obtained after 40 min at the OCP, fitted to an equivalent circuit $R_s(R_{ct}Q)$. The fitted curves are lines and the markers are experimental data. (b) Polarization curves recorded in 0.05 M H_2SO_4 at a scan rate of 5 mV/s.

formed under OCP conditions. These results confirm that the presence of carbon significantly improved the corrosion properties of the CoCrFeMnNi thin films. The EIS spectra can be fitted to the simple equivalent circuit model of $R_s(R_{ct}Q)$ using the EC-lab software. The fitted curves are seen in Fig 9(a) as lines over each set of experimental data. In this model, the R_s represents the electrolyte resistance and the R_{ct} is the charge transfer resistance, which is inversely proportional to the corrosion rate. The R_{ct} increased from 0.6 MΩ to 3.5 MΩ with the carbon content (SI Table 6), confirming that the carbon-free sample corroded more easily. Q is the constant phase element (CPE) which represents a shift from ideal capacitive behavior. The impedance of the CPE is expressed by $Z_Q = Y_0^{-1}(j\omega)^{-n}$, where Z_Q is the CPE impedance value (Ω), Y_0 is the CPE constant which represents the capacitance part in CPE, $j=(-1)^{1/2}$ which is equal to the imaginary number, ω is the angular frequency in rad/s and n is a dimensionless constant related to the roughness of the surface [65], with values between 0 and 1. When n = 0, the CPE becomes equivalent to a resistor while for n = 1, the CPE becomes equivalent to an ideal capacitor [66]. The simulated values of n increase from 0.90 for the carbon-free sample to 0.93 and 0.94 for 6 and 11 at.% carbon, respectively. This confirms the more capacitive behavior of the carbon-containing films. The lower n value for the carbon-free sample can also be related to a difference in surface roughness, as the carbon-free sample seems to have a slightly higher roughness (SI Fig. 2).

Following the experimental procedure thus far, we have observed the formation of a Cr-rich surface oxide layer on each of the samples. The subsequent polarization experiment, performed directly after the EIS, was designed to test the performance of this oxide layer. This was achieved by using a short cathodic region, to limit the reduction of the oxide. A more extensive reduction (i.e. the use of a wider cathodic potential range) would mean that the polarization curve mainly would reflect the formation of a new passive layer. Since, in a real-life application, the surface oxide layer will never be fully reduced, keeping the OCP oxide layer intact is closer to a real-life corrosion situation, e.g. in a fuel cell. The polarization experiments were started at −0.3 vs. the OCP, and the results are shown in Fig. 8(b).

The shape of the early part of the polarization curve further confirms the results of the prior steps, showing that the films with more carbon formed a more corrosion resistant passive layer at the OCP. The corrosion potential (E_{corr}, see Table 2) was shifted to progressively higher values upon increasing the carbon content, i.e. −0.28 V, −0.21 V, and −0.18 V vs. Ag/AgCl, for 0, 6, and 11 at.% C, respectively. Meanwhile, the corrosion current density (j_{corr}) decreased with increasing carbon content, $8{\cdot}10^{-6}$, $9{\cdot}10^{-7}$, and $8{\cdot}10^{-8}$ A/cm^2 for 0, 6, and 11 at.% C, respectively. A higher E_{corr} value and lower j_{corr} value in the same electrolyte indicate that the corrosion reaction is slower. The XPS results showed that there was almost no difference in the relative intensities of the different metals close to the surface before the polarization experiment was started. As the behavior of the metals during corrosion appears to be the same, the slower corrosion reactions must be due to the presence of carbon. For comparison, the sample with 11 at.% C exhibited similar E_{corr} and j_{corr} values as a hyper-duplex stainless steel (Sandvik-SAF 3207 HD [67]), developed for highly corrosive environments (see supporting information SI Fig. 5).

The carbon-containing samples also had lower current densities than the carbon-free sample in the passive region, i.e. from E_{corr} to around 0.8 V vs. Ag/AgCl. The region with a lower current was shorter for the sample with 6 at.% C and longer for the one with 11 at.% C. For 6 at.%, the current density was as high as for the carbon-free sample from 0.4 V and onward, while the sample with 11 at.% C featured a longer interval with a lower current, extending up to 0.8 V. This is another strong indication that it was the presence of carbon that gave rise to improved corrosion resistance. To further study this effect, ICP-MS experiments were performed on the electrolyte after polarizing the samples with 0 and 11 at.% C at 0.4 V vs. Ag/AgCl for two hours. The results of these experiments, which are presented in the supporting information (SI Table 4), show that the overall metal concentration in the electrolyte was 35% lower for the sample with 11 at.% C, compared to the carbon-free sample. The relative amounts of Cr, Fe, and Co were similar to the values found after the OCP, but Mn was found at lower concentrations and Ni at higher. All the metallic elements were found at lower concentrations for the sample with 11 at.% C, indicating that the presence of carbon slows down the dissolution of the oxide films, without a dramatic change in the behavior of the metals.

At potentials beyond 0.8 V (Fig. 8(b)), there was a rapid increase in the current density for all three samples. This can be explained by the Cr(III) species in the passive layer being oxidized to soluble Cr(VI) species [61], as in the trans-passive region of stainless steels. As a potential of 1.3 V was reached, the current density for the carbon-free sample decreased dramatically while it continued to increase for the two carbon-containing samples. The ICP-MS results obtained after polarization at 1.3 V for two hours, show around three times higher concentrations of metal ions in the electrolyte exposed to the 11 at.% C sample than the carbon-free sample (SI Table 5). Based on the Pourbaix diagram for Mn [61], the decrease in the current for the carbon-free sample could be explained by the formation of a passive layer composed of manganese(IV)oxide. This is also supported by the lower relative amount of Mn ions in the electrolyte, compared to all other metallic elements. The lower manganese content in the carbon-containing samples (see Table 1) could not explain the absence of this second passivation, as non-equimolar bulk samples with similar Mn concentrations (the composition was $Cr_{21}Mn_{10}Fe_{23}Co_{23}Ni_{23}$) were tested in the same way, and exhibited the same current decrease at 1.3 V. The higher currents in the carbon-containing samples could partly be due to the oxidation of carbon. However, this does not explain why the sample with carbon released higher amounts of metals to the solution, as found by ICP-MS. Further studies are needed to explain why the Mn oxide passivation only was seen for the carbon-free sample.

Amorphous films were formed upon the addition of carbon. The corrosion behavior of amorphous alloys is a well-discussed topic, with some claiming that they should have a higher resistance than crystalline alloys, and others claiming the opposite. No such general principles have yet been proven, but a common observation is that the lower defect concentration and higher chemical homogeneity of amorphous alloys can yield lower corrosion rates compared to crystalline alloys of similar composition [68,69]. These differences can be large between amorphous and crystalline bulk alloys. However, using magnetron sputtering, amorphous and crystalline films with similar elemental segregation and morphology can be acquired. Given the results from the SEM images in SI Fig. 2, showing low roughness and high density for both films, and the TEM-EDX maps (supporting information, SI Fig. 3) showing no detectable segregation for either, we can assume that the observed increase in corrosion resistance does not depend on these factors. The improvement in corrosion performance between the samples with 6% C and 11% C, considering that both these films were amorphous, further indicates that the change from crystalline to amorphous cannot be the only cause of the improved performance.

The differences are better explained by the behavior of carbon during the corrosion process. Thermodynamically, CO_2 should be formed above 0 V vs. Ag/AgCl [61]. However, the rate of oxidation is relatively low, which is why carbon can be used in corrosive environments. During the corrosion of graphite, it was reported that CO_2, CO, and oxidized surface groups were formed in parallel

above around 0.3 V vs. Ag/AgCl [70]. The results of studies on sputtered Cr-C thin films [11,47] suggest that, when the carbide phase is oxidized, carbon remains on the surface during the formation of Cr_2O_3. The carbon, being relatively inert, oxidizes slowly and therefore inhibits corrosion. Even when the carbon is oxidized, it can remain on the surface as oxidized (i.e. oxygen-containing) groups.

In this study, the concentration of carbon is much lower than in the Cr-C films, but as the metallic elements are dissolved, carbon should become enriched in the material. During the OCP, the more noble Ni was oxidized to a lesser extent and was therefore enriched below the oxide film. The same principle should apply to carbon, as it has a higher standard potential than any of the metals, and typically corrodes more slowly. After 40 min at the OCP, the films with carbon have orders of magnitude lower corrosion currents, showing that this enrichment greatly inhibits the corrosion process. During the polarization curve (Fig. 8(b)), above a certain potential, the protective effect from carbon becomes less pronounced. However, the effect remains up to higher potentials for the film with 11 at.% C than for the one with 6 at.% C. It seems that there is the possibility of improving the corrosion resistance further by increasing the carbon content. A more in-depth corrosion study, coupled with studies of the oxidized surface, would help to investigate this protective mechanism and hopefully to pinpoint the location and function of the carbon enrichment.

4. Conclusions

Equimolar CoCrFeMnNi thin films with different carbon concentrations were deposited by magnetron sputtering and characterized with regard to mechanical properties and corrosion resistance. A summary of all material properties is presented in Table 2. The conclusions are:

1. According to the thermodynamic calculations, the equimolar CoCrFeMnNi with added carbon forms a phase mixture of alloy and metal carbide phases at equilibrium, accompanied by segregation of the metallic elements.
2. Experimentally, it was found that the addition of carbon formed an amorphous material with 6 and 11 at.% C, as shown by X-ray and electron diffraction. No signs of a segregated carbide were detected by diffraction or by EDX, and XPS showed that the carbon was almost entirely found in a metallic environment. The suppression of the carbide formation is explained by the fast quenching and limited atomic diffusion during the sputter deposition, in combination with the many weak carbide forming elements in the alloy.
3. The addition of carbon to CoCrFeMnNi caused an increase in hardness, shown by nanoindentation. This effect is tied to the shift from crystalline to amorphous.
4. Coating fragmentation in tensile testing showed its versatility by revealing multiple cracks in CrFeMnCoNi films; it is a suitable method for comparing ductile thin films. The results show that the strength of the films increased upon carbon addition. The carbon also gave rise to a more heterogeneous film material, which was manifested by a larger scatter in the strain at crack onset as well as the continued cracking behavior. Both effects are tied to the shift from crystalline to amorphous.
5. The corrosion resistance of the films increased with increasing carbon content, up to about 0.8 V vs. Ag/AgCl, as shown by the electrochemical results. The presence of carbon close to the surface of the films appeared to be the main reason for this improvement. At potentials above 1.3 V vs. Ag/AgCl, the carbon-free film exhibited a second passivation due to the formation of Mn(IV) oxide. The corrosion resistance for the sample with 11 at.% C is slightly higher than for a hyper-duplex stainless steel designed for highly corrosive conditions.

The results show that the addition of carbon increased the corrosion resistance and enhanced both the crack resistance and hardness. This brings us closer to finding the multifunctional material that is needed for corrosion-resistant coatings, for example on bipolar plates in PEM fuel cells. A deeper understanding of the deformation and corrosion mechanisms is needed to generalize this approach and, in the future, apply it to other material systems.

CRediT authorship contribution statement

León Zendejas Medina: Conceptualization, Investigation, Formal analysis, Writing - original draft. **Marcus V. Tavares da Costa:** Methodology, Investigation, Formal analysis, Writing - original draft. **E. Maria Paschalidou:** Investigation, Formal analysis, Writing - original draft. **Greta Lindwall Methodolody:** Formal analysis, Writing - original draft. **Lars Riekehr:** Investigation, Formal analysis, Writing - original draft. **Marcus Korvela:** Investigation, Formal analysis, Writing - review & editing. **Stefan Fritze:** Investigation, Formal analysis, Writing - review & editing. **Greta Lindwall:** Methodology, Formal analysis, Writing - original draft. **Szilárd Kolozsvári :** Methodolody, Investigation, Formal analysis, Writing - review & editing. **E. Kristofer Gamstedt:** Writing - review & editing. **Leif Nyholm:** Conceptualization, Writing - review & editing. **Ulf Jansson:** Conceptualization, Writing - review & editing.

Declaration of Competing Interest

The authors declare that they have no known competing financial interests or personal relationships that could have appeared to influence the work reported in this paper.

Acknowledgments

We would like to acknowledge the Tandem Laboratory for their assistance with ion beam analysis. The operation of the Tandem accelerator at Uppsala University is supported by the Swedish research council, VR-RFI [contracts #821-2012-5144 & #2017-00646_9], and the Swedish Foundation for Strategic Research (SSF) [contract RIF14-0053]. We also thank Rebecka Lindblad for her support in fitting the XPS data. The Swedish Research Council (VR) is gratefully acknowledged [project 2018-04834]. This study was performed in the framework of the competence center FunMat-II that is financially supported by Vinnova [grant no 2016-05156].

Data availability

The data that support the findings of this study are available from the corresponding author upon request.

Appendix A. Supplementary data

Supplementary data to this article can be found online at https://doi.org/10.1016/j.matdes.2021.109711.

References

[1] B. Cantor, I.T.H. Chang, P. Knight, A.J.B. Vincent, Microstructural development in equiatomic multicomponent alloys, Mater. Sci. Eng. A. 375–377 (2004) 213–218, https://doi.org/10.1016/j.msea.2003.10.257.
[2] D.B. Miracle, O.N. Senkov, A critical review of high entropy alloys and related concepts, Acta Mater. 122 (2017) 448–511, https://doi.org/10.1016/J.ACTAMAT.2016.08.081.
[3] J.E. Saal, I.S. Berglund, J.T. Sebastian, P.K. Liaw, G.B. Olson, Equilibrium high entropy alloy phase stability from experiments and thermodynamic modeling, Scr. Mater. 146 (2018) 5–8, https://doi.org/10.1016/j.scriptamat.2017.10.027.

[4] V. Pacheco, G. Lindwall, D. Karlsson, J. Cedervall, S. Fritze, G. Ek, P. Berastegui, M. Sahlberg, U. Jansson, Thermal Stability of the HfNbTiVZr High-Entropy Alloy, Inorg. Chem. 58 (2019) 811–820, https://doi.org/10.1021/acs.inorgchem.8b02957.
[5] L. Zendejas Medina, L. Riekehr, U. Jansson, Phase formation in magnetron sputtered CrMnFeCoNi high entropy alloy, Surf. Coatings Technol. 403 (2020), https://doi.org/10.1016/j.surfcoat.2020.126323 126323.
[6] B. Gludovatz, A. Hohenwarter, D. Catoor, E.H. Chang, E.P. George, R.O. Ritchie, A fracture-resistant high-entropy alloy for cryogenic applications, Science (80-.). 345 (2014) 1153–1158. http://doi.org/10.1126/science.1254581.
[7] H. Luo, Z. Li, A.M. Mingers, D. Raabe, Corrosion behavior of an equiatomic CoCrFeMnNi high-entropy alloy compared with 304 stainless steel in sulfuric acid solution, Corros. Sci. 134 (2018) 131–139, https://doi.org/10.1016/j.corsci.2018.02.031.
[8] J. Wu, X.Z. Yuan, J.J. Martin, H. Wang, J. Zhang, J. Shen, S. Wu, W. Merida, A review of PEM fuel cell durability: Degradation mechanisms and mitigation strategies, J. Power Sources. 184 (2008) 104–119, https://doi.org/10.1016/j.jpowsour.2008.06.006.
[9] A. Hermann, T. Chaudhuri, P. Spagnol, Bipolar plates for PEM fuel cells: A review, Int. J. Hydrogen Energy. 30 (2005) 1297–1302, https://doi.org/10.1016/j.ijhydene.2005.04.016.
[10] J. Chen, Z. Yao, X. Wang, Y. Lu, X. Wang, Y. Liu, X. Fan, Effect of C content on microstructure and tensile properties of as-cast CoCrFeMnNi high entropy alloy, Mater. Chem. Phys. 210 (2018) 136–145, https://doi.org/10.1016/j.matchemphys.2017.08.011.
[11] J. Högström, M. Andersson, U. Jansson, F. Björefors, L. Nyholm, On the evaluation of corrosion resistances of amorphous chromium-carbon thin-films, Electrochim. Acta. 122 (2014) 224–233, https://doi.org/10.1016/j.electacta.2013.11.130.
[12] H. Luo, S. Zou, Y.H. Chen, Z. Li, C. Du, X. Li, Influence of carbon on the corrosion behaviour of interstitial equiatomic CoCrFeMnNi high-entropy alloys in a chlorinated concrete solution, Corros. Sci. 163 (2020), https://doi.org/10.1016/j.corsci.2019.108287.
[13] L. Yang, C. Liu, M. Wen, X. Dai, Y. Zhang, X. Chen, K. Zhang, Small atoms as reinforced agent for both hardness and toughness of Group-VIB transition metal films, J. Alloys Compd. 735 (2018) 1105–1110, https://doi.org/10.1016/j.jallcom.2017.11.208.
[14] S. Fritze, P. Malinovskis, L. Riekehr, L. von Fieandt, E. Lewin, U. Jansson, Hard and crack resistant carbon supersaturated refractory nanostructured multicomponent coatings, Sci. Rep. 8 (2018) 1–8, https://doi.org/10.1038/s41598-018-32932-y.
[15] U. Jansson, E. Lewin, Carbon-containing multi-component thin films, Thin Solid Films. 688 (2019), https://doi.org/10.1016/j.tsf.2019.137411 137411.
[16] S. Fritze, M. Hans, L. Riekehr, B. Osinger, E. Lewin, J.M. Schneider, U. Jansson, Influence of carbon on microstructure and mechanical properties of magnetron sputtered TaW coatings, Mater. Des. 196 (2020), https://doi.org/10.1016/j.matdes.2020.109070 109070.
[17] S.R. Shatynski, The thermochemistry of transition metal carbides, Oxid. Met. 13 (1979) 105–118, https://doi.org/10.1007/BF00611975.
[18] S. Chen, L. Liu, T. Wang, Investigation of the mechanical properties of thin films by nanoindentation, considering the effects of thickness and different coating-substrate combinations, Surf. Coatings Technol. 191 (2005) 25–32, https://doi.org/10.1016/j.surfcoat.2004.03.037.
[19] M.V. Tavares da Costa, C. Neagu, P. Fayet, U. Wiklund, H. Li, K. Leifer, E.K. Gamstedt, Comparison of test methods estimating the stiffness of ultrathin coatings, J. Coatings Technol. Res. 15 (2018) 743–752, https://doi.org/10.1007/s11998-018-0085-0.
[20] W.C. Oliver, G.M. Pharr, An improved technique for determining hardness and elastic modulus using load and displacemenent sensing indentation experiments, J. Mater. Res. 7 (1992) 1564–1583, https://doi.org/10.1557/JMR.1992.1564.
[21] X. Chen, Y. Du, Y.W. Chung, Commentary on using H/E and H3/E2 as proxies for fracture toughness of hard coatings, Thin Solid Films. 688 (2019), https://doi.org/10.1016/j.tsf.2019.04.040 137265.
[22] K. Fu, Y. Yin, L. Chang, D. Shou, B. Zheng, L. Ye, Analysis on multiple ring-like cracks in thin amorphous carbon film on soft substrate under nanoindentation, J. Phys. D. Appl. Phys. 46 (2013), https://doi.org/10.1088/0022-3727/46/50/505314.
[23] S. Zhang, D. Sun, Y. Fu, H. Du, Toughness measurement of thin films: A critical review, Surf. Coatings Technol. 198 (2005) 74–84, https://doi.org/10.1016/j.surfcoat.2004.10.021.
[24] J. Ast, M. Ghidelli, K. Durst, M. Göken, M. Sebastiani, A.M. Korsunsky, A review of experimental approaches to fracture toughness evaluation at the micro-scale, Mater. Des. 173 (2019), https://doi.org/10.1016/j.matdes.2019.107762 107762.
[25] M.V. Tavares da Costa, J. Bolinsson, R.C. Neagu, P. Fayet, E.K. Gamstedt, Experimental assessment of micromechanical models for fragmentation analysis of thin metal oxide coatings on polymer films under uniaxial tensile deformation, Surf. Coatings Technol. 370 (2019) 374–383, https://doi.org/10.1016/j.surfcoat.2019.03.035.
[26] F. Meng, J.L. David, S. Bollin, M.E. Nichols, M.D. Thouless, Kinetics of channeling cracks in polymeric coatings, Int. J. Solids Struct. 132–133 (2018) 105–113, https://doi.org/10.1016/j.ijsolstr.2017.09.023.
[27] M.J. Cordill, A. Taylor, J. Schalko, G. Dehm, Fracture and delamination of chromium thin films on polymer substrates, in: Metall. Mater. Trans. A Phys. Metall. Mater. Sci., Springer, 2010: pp. 870–875. http://doi.org/10.1007/s11661-009-9988-9.
[28] Y. Leterrier, Y. Wyser, J.A.E. Månson, J. Hilborn, A Method to Measure the Adhesion of Thin Glass Coatings on Polymer Films, J. Adhes. 44 (1994) 213–227, https://doi.org/10.1080/00218469408027078.
[29] J.L. Beuth, Cracking of thin bonded films in residual tension, Int. J. Solids Struct. 29 (1992) 1657–1675, https://doi.org/10.1016/0020-7683(92)90015-L.
[30] J.O. Andersson, T. Helander, L. Höglund, P. Shi, B. Sundman, Thermo-Calc & DICTRA, computational tools for materials science, Calphad Comput. Coupling Phase Diagrams Thermochem. 26 (2002) 273–312, https://doi.org/10.1016/S0364-5916(02)00037-8.
[31] H.L. Chen, H. Mao, Q. Chen, Database development and Calphad calculations for high entropy alloys: Challenges, strategies, and tips, Mater. Chem. Phys. 210 (2018) 279–290, https://doi.org/10.1016/j.matchemphys.2017.07.082.
[32] T.-C. Software, TCHEA3: TCS High Entropy Alloy Database, (2018). https://www.thermocalc.com/media/35873/tchea3_extended_info.pdf (accessed December 16, 2019).
[33] M. Klinger, CrysTBox - Crystallographic Toolbox., (2015). http://www.fzu.cz/~klinger/crystbox.pdf.
[34] P. Stadelmann, JEMS Java Electron Microscopy Software, 2004, (n.d.).
[35] Q. An, S. Tamrakar, J.W. Gillespie, A.N. Rider, E.T. Thostenson, Tailored glass fiber interphases via electrophoretic deposition of carbon nanotubes: Fiber and interphase characterization, Compos. Sci. Technol. 166 (2018) 131–139, https://doi.org/10.1016/j.compscitech.2018.01.003.
[36] D.B. Bogy, Edge-bonded dissimilar orthogonal elastic wedges under normal and shear loading, J. Appl. Mech. Trans. ASME. 35 (1964) 460–466, https://doi.org/10.1115/1.3601236.
[37] S.V. Meschel, O.J. Kleppa, Standard enthalpies of formation of some 3d transition metal carbides by high temperature reaction calorimetry, J. Alloys Compd. 257 (1997) 227–233, https://doi.org/10.1016/S0925-8388(97)00023-6.
[38] C. Zhang, M.C. Gao, CALPHAD modeling of high-entropy alloys, in: High-Entropy Alloy. Fundam. Appl., Springer International Publishing, 2016: pp. 399–444. http://doi.org/10.1007/978-3-319-27013-5_12.
[39] F. Kies, X. Wu, B. Hallstedt, Z. Li, C. Haase, Enhanced precipitation strengthening of multi-principal element alloys by κ- and B2-phases, Mater. Des. 198 (2021), https://doi.org/10.1016/j.matdes.2020.109315 109315.
[40] M. Vaidya, A. Karati, K. Guruvidyathri, M. Nagini, K.G. Pradeep, B.S. Murty, Suppression of σ-phase in nanocrystalline CoCrFeMnNiV high entropy alloy by unsolicited contamination during mechanical alloying and spark plasma sintering, Mater. Chem. Phys. 255 (2020), https://doi.org/10.1016/j.matchemphys.2020.123558 123558.
[41] T. Nagase, T. Kakeshita, K. Matsumura, K. Nakazawa, S. Furuya, N. Ozoe, K. Yoshino, Development of Fe-Co-Cr-Mn-Ni-C high entropy cast iron (HE cast iron) available for casting in air atmosphere, Mater. Des. 184 (2019), https://doi.org/10.1016/j.matdes.2019.108172 108172.
[42] S. Fujimoto, R.C. Newman, G.S. Smith, S.P. Kaye, H. Kheyrandish, J.S. Colligon, Passivation thresholds in iron-chromium alloys prepared by ion-beam sputtering, Corros. Sci. 35 (1993) 51–55, https://doi.org/10.1016/0010-938X(93)90132-Z.
[43] M. Vaidya, K.G. Pradeep, B.S. Murty, G. Wilde, S.V. Divinski, Bulk tracer diffusion in CoCrFeNi and CoCrFeMnNi high entropy alloys, Acta Mater. 146 (2018) 211–224, https://doi.org/10.1016/j.actamat.2017.12.052.
[44] Y.J. Li, A. Savan, A. Kostka, H.S. Stein, A. Ludwig, Accelerated atomic-scale exploration of phase evolution in compositionally complex materials, Mater. Horizons. 5 (2018) 86–92, https://doi.org/10.1039/c7mh00486a.
[45] A.L. Greer, Y.Q. Cheng, E. Ma, Shear bands in metallic glasses, Mater. Sci. Eng. R Reports. 74 (2013) 71–132, https://doi.org/10.1016/j.mser.2013.04.001.
[46] T. Suszko, W. Gulbiński, J. Morgiel, G. Greczynski, E. Dobruchowska, P. Dłużewski, J. Lu, L. Hultman, Amorphous FeCrNi/a-C: H coatings with self-organizednanotubular structure, Scr. Mater. 136 (2017) 24–28, https://doi.org/10.1016/j.scriptamat.2017.03.040.
[47] K. Nygren, M. Andersson, J. Högström, W. Fredriksson, K. Edström, L. Nyholm, U. Jansson, Influence of deposition temperature and amorphous carbon on microstructure and oxidation resistance of magnetron sputtered nanocomposite CrC films, Appl. Surf. Sci. 305 (2014) 143–153, https://doi.org/10.1016/j.apsusc.2014.03.014.
[48] A. Furlan, U. Jansson, J. Lu, L. Hultman, M. Magnuson, Structure and bonding in amorphous iron carbide thin films, J. Phys. Condens. Matter. 27 (2015) 1, https://doi.org/10.1088/0953-8984/27/4/045002.
[49] J.F. Moulder, W.F. Stickle, P.E. Sobol, K.D. Bomben, Handbook of X-ray photoelectron spectroscopy (1995), https://doi.org/10.1002/sia.740030412.
[50] M. Detroye, F. Reniers, C. Buess-Herman, J. Vereecken, AES-XPS study of chromium carbides and chromium iron carbides, Appl. Surf. Sci. 144–145 (1999) 78–82, https://doi.org/10.1016/S0169-4332(98)00769-7.
[51] F. Maury, D. Oquab, J.C. Manse, R. Morancho, J.F. Nowak, J.P. Gauthier, Structural characterization of chromium carbide coatings deposited at low temperature by low pressure chemical vapour decomposition using dicumene chromium, Surf. Coatings Technol. 41 (1990) 51–61, https://doi.org/10.1016/0257-8972(90)90129-Z.
[52] G.B. Hoflund, D.A. Asbury, S.J. Babb, A.L. Grogan, H.A. Laitinen, S. Hoshino, A surface study of amorphous chromium films electrodeposited from chromic acid solutions, Part I, J. Vac. Sci. Technol. A Vacuum, Surfaces, Film. 4 (1986) 26–30, https://doi.org/10.1116/1.573493.
[53] U. Jansson, E. Lewin, Sputter deposition of transition-metal carbide films - A critical review from a chemical perspective, Thin Solid Films. 536 (2013) 1–24, https://doi.org/10.1016/j.tsf.2013.02.019.

[54] B. Trindade, M.T. Vieira, Modification of the structural order of transition metal-carbon systems by the addition of a Group VIII element, Mater. Sci. Eng. A. 352 (2003) 195–201, https://doi.org/10.1016/S0921-5093(02)00865-1.
[55] D. Shinde, S. Fritze, M. Thuvander, P. Malinovskis, L. Riekehr, U. Jansson, K. Stiller, Elemental Distribution in CrNbTaTiW-C High Entropy Alloy Thin Films, Microsc. Microanal. 25 (2019) 489–500, https://doi.org/10.1017/S1431927618016264.
[56] C.A. Schuh, T.G. Nieh, A nanoindentation study of serrated flow in bulk metallic glasses, Acta Mater. 51 (2003) 87–99, https://doi.org/10.1016/S1359-6454(02)00303-8.
[57] M. Hurakova, K. Csach, J. Miskuf, A. Jurikova, S. Demcak, V. Ocelik, J.T.M.D. Hosson, Discontinuities of Plastic Deformation in Metallic Glasses with Different Glass Forming Ability, Phys. Procedia, Elsevier B.V. (2015) 1265–1270, https://doi.org/10.1016/j.phpro.2015.12.140.
[58] Y. Leterrier, J. Andersons, Y. Pitton, J.-A.E. Månson, Adhesion of silicon oxide layers on poly(ethylene terephthalate). II: Effect of coating thickness on adhesive and cohesive strengths, J. Polym. Sci. Part B Polym. Phys. 35 (1997) 1463–1472, https://doi.org/10.1002/(SICI)1099-0488(19970715)35:9<1463::AID-POLB16>3.0.CO;2-4.
[59] C. Giolli, A. Scrivani, G. Rizzi, F. Borgioli, G. Bolelli, L. Lusvarghi, Failure mechanism for thermal fatigue of thermal barrier coating systems, in: J. Therm. Spray Technol., Springer, 2009: pp. 223–230. http://doi.org/10.1007/s11666-009-9307-4.
[60] C. Wan, W. Yang, H. Liu, M. Zuo, Q. Li, Z. Ma, Y. Zhao, A. Inoue, Ductile Fe-based bulk metallic glasses at room temperature, Mater. Sci. Technol. 34 (2018) 751–756, https://doi.org/10.1080/02670836.2017.1412037.
[61] M. Pourbaix, Atlas of Electrochemical equilibria in aqueous solutions, NACE International Cebelcor (1974).
[62] C.O.A. Olsson, D. Landolt, Passive films on stainless steels - Chemistry, structure and growth, Electrochim. Acta. 48 (2003) 1093–1104, https://doi.org/10.1016/S0013-4686(02)00841-1.
[63] L. Wang, D. Mercier, S. Zanna, A. Seyeux, M. Laurent-Brocq, L. Perrière, I. Guillot, P. Marcus, L. Perriere, I. Guillot, P. Marcus, Study of the surface oxides and corrosion behaviour of an equiatomic CoCrFeMnNi high entropy alloy by XPS and ToF-SIMS, Corros. Sci. 167 (2020), https://doi.org/10.1016/j.corsci.2020.108507 108507.
[64] G. Greczynski, L. Hultman, C 1s Peak of Adventitious Carbon Aligns to the Vacuum Level: Dire Consequences for Material's Bonding Assignment by Photoelectron Spectroscopy, ChemPhysChem. 18 (2017) 1507–1512, https://doi.org/10.1002/cphc.201700126.
[65] L. Nyikos, T. Pajkossy, Fractal dimension and fractional power frequency-dependent impedance of blocking electrodes, Electrochim. Acta. 30 (1985) 1533–1540, https://doi.org/10.1016/0013-4686(85)80016-5.
[66] A.A. Sagüés, S.C. Kranc, E.I. Moreno, The time-domain response of a corroding system with constant phase angle interfacial component: Application to steel in concrete, Corros. Sci. 37 (1995) 1097–1113, https://doi.org/10.1016/0010-938X(95)00017-E.
[67] P. Malinovskis, S. Fritze, L. Riekehr, L. von Fieandt, J. Cedervall, D. Rehnlund, L. Nyholm, E. Lewin, U. Jansson, Synthesis and characterization of multicomponent (CrNbTaTiW)C films for increased hardness and corrosion resistance, Mater. Des. 149 (2018) 51–62, https://doi.org/10.1016/j.matdes.2018.03.068.
[68] C. Suryanarayana, A. Inoue, Iron-based bulk metallic glasses, Int. Mater. Rev. 58 (2013) 131–166, https://doi.org/10.1179/1743280412Y.0000000007.
[69] Y. Waseda, K.T. Aust, Corrosion behaviour of metallic glasses, J. Mater. Sci. 16 (1981) 2337–2359, https://doi.org/10.1007/BF01113569.
[70] F. Maillard, W.O. Silva, L. Castanheira, L. Dubau, F.H.B. Lima, Carbon Corrosion in Proton-Exchange Membrane Fuel Cells: Spectrometric Evidence for Pt-Catalysed Decarboxylation at Anode-Relevant Potentials, ChemPhysChem. 20 (2019) 3106–3111, https://doi.org/10.1002/cphc.201900505.